



# Development of allosteric and selective CDK2 inhibitors for contraception with negative cooperativity to cyclin binding

Received: 18 July 2022

Accepted: 12 May 2023

Published online: 03 June 2023

Check for updates

Erik B. Faber<sup>1,2,3</sup>, Luxin Sun<sup>4</sup>, Jian Tang<sup>1</sup>, Emily Roberts<sup>5</sup>, Sornakala Ganeshkumar<sup>5</sup>, Nan Wang<sup>1,2</sup>, Damien Rasmussen<sup>6,7</sup>, Abir Majumdar<sup>6</sup>, Laura E. Hirsch<sup>1</sup>, Kristen John<sup>1,2</sup>, An Yang<sup>1,2</sup>, Hira Khalid<sup>1,2</sup>, Jon E. Hawkinson<sup>1,2</sup>, Nicholas M. Levinson<sup>6</sup>, Vargheese Chennathukuzhi<sup>5</sup>, Daniel A. Harki<sup>1</sup>, Ernst Schönbrunn<sup>4</sup> & Gunda I. Georg<sup>1,2</sup> ✉

Compared to most ATP-site kinase inhibitors, small molecules that target an allosteric pocket have the potential for improved selectivity due to the often observed lower structural similarity at these distal sites. Despite their promise, relatively few examples of structurally confirmed, high-affinity allosteric kinase inhibitors exist. Cyclin-dependent kinase 2 (CDK2) is a target for many therapeutic indications, including non-hormonal contraception. However, an inhibitor against this kinase with exquisite selectivity has not reached the market because of the structural similarity between CDKs. In this paper, we describe the development and mechanism of action of type III inhibitors that bind CDK2 with nanomolar affinity. Notably, these anthranilic acid inhibitors exhibit a strong negative cooperative relationship with cyclin binding, which remains an underexplored mechanism for CDK2 inhibition. Furthermore, the binding profile of these compounds in both biophysical and cellular assays demonstrate the promise of this series for further development into a therapeutic selective for CDK2 over highly similar kinases like CDK1. The potential of these inhibitors as contraceptive agents is seen by incubation with spermatocyte chromosome spreads from mouse testicular explants, where they recapitulate *Cdk2*<sup>-/-</sup> and *Spdy1*<sup>-/-</sup> phenotypes.

Kinases remain attractive therapeutic targets to treat a variety of diseases, but with over 500 kinases in the human proteome, the selective targeting of a particular kinase remains challenging. This is in large part due to the structural similarity among kinases, especially at the ATP-site where most kinase inhibitors bind. To meet this challenge, a variety of strategies have emerged including developing inhibitors that

either bind unique inactive conformations, target unique residues including nucleophilic residues for covalent attachment<sup>1</sup>, or are heterobifunctional and lead to kinase degradation<sup>2</sup>. In addition, allosteric type III inhibitors, compounds that bind the kinase outside of the active site, have been a promising avenue to selectively inhibit kinases as these distal sites often have reduced structural similarity. Some

<sup>1</sup>Department of Medicinal Chemistry, University of Minnesota College of Pharmacy—Twin Cities, Minneapolis, MN, USA. <sup>2</sup>Institute for Therapeutics Discovery and Development, University of Minnesota College of Pharmacy—Twin Cities, Minneapolis, MN, USA. <sup>3</sup>Medical Scientist Training Program, University of Minnesota Medical School—Twin Cities, Minneapolis, MN, USA. <sup>4</sup>Drug Discovery Department, Moffitt Cancer Center, Tampa, FL, USA. <sup>5</sup>Department of Molecular and Integrative Physiology, Institute for Reproductive and Developmental Sciences, University of Kansas Medical Center, Kansas City, KS, USA. <sup>6</sup>Department of Pharmacology, University of Minnesota Medical School—Twin Cities, Minneapolis, MN, USA. <sup>7</sup>Department of Biochemistry, Molecular Biology & Biophysics, University of Minnesota Medical School—Twin Cities, Minneapolis, MN, USA. ✉e-mail: [georg@umn.edu](mailto:georg@umn.edu)

allosteric kinase inhibitors even demonstrate selectivity for oncologic mutant isoforms of the same kinase<sup>3–5</sup>. To date, four allosteric kinase inhibitors have been approved by the U.S. Food and Drug Administration to treat BRAF-mutated cancers and recently asciminib was approved as a treatment for chronic myeloid leukemia targeting an allosteric pocket of ABL kinase<sup>6–10</sup>. Despite this success, few high affinity and well-characterized allosteric kinase inhibitors have been reported in the literature<sup>11,12</sup>. In this paper, we will showcase a series of anthranilic acid-derived inhibitors that bind an allosteric pocket of cyclin-dependent kinase 2 (CDK2) with nanomolar affinity.

CDK2 is a member of the CDK family of kinases that control the cell cycle and is activated by binding E-type cyclins at the G1-S transition, then by A-type cyclins in S phase. In addition, CDK2 must be phosphorylated on the activation loop to become fully activated. CDK2 also plays a critical role in meiosis since *Cdk2*<sup>-/-</sup> mice are sterile but otherwise healthy<sup>13,14</sup>, making CDK2 a validated target for non-hormonal contraceptive development<sup>15</sup>. In meiosis, the protein Speedy1 (SPY1) binds unphosphorylated CDK2 at the same site where cyclins bind<sup>16</sup> and appears to be the crucial binding partner of CDK2 in the pachytene stage of prophase I<sup>17</sup>. While the *Cdk2*<sup>-/-</sup> phenotype suggests a selective CDK2 inhibitor will have a favorable safety profile, further investigation reveals that selective inhibition of CDK2/cyclin complexes can be relatively toxic for healthy cells due to the sequestration of cyclins and thus the loss of compensatory kinase activation<sup>18</sup>. However, a compound that disrupts the protein-protein interaction (PPI) between CDK2 and its protein partners like cyclin or SPY1 has the potential to be an alternative, less toxic CDK2 inhibitor. In this manner, an ideal inhibitor would free cyclins normally bound to CDK2, leading to A) the activation of compensatory kinases by displaced cyclins in somatic cells and B) disruption of the CDK2/SPY1 interaction crucial for meiosis in spermatocytes, providing a safe and efficacious contraceptive option.

We previously discovered that the dye 8-anilino-1-naphthalene sulfonic acid (ANS) bound an unrecognized allosteric pocket within CDK2 with moderate affinity with a 5–10-fold enhancement in affinity in the presence of certain orthosteric inhibitors<sup>19,20</sup>. Despite this promise, ANS is known to be a promiscuous protein binder<sup>21–25</sup> and contains a sulfonic acid moiety that confers poor pharmacokinetic properties. However, we exploited the environmentally sensitive fluorescent nature of ANS to develop a high-throughput assay and used it to discover new chemical scaffolds with improved physicochemical properties that bind the allosteric pocket with higher affinity<sup>26,27</sup>. From those efforts, we herein reveal the highest affinity allosteric CDK2 inhibitors reported, all containing an anthranilic acid scaffold. We confirm their type III allosteric interaction by X-ray crystallography and use other biophysical techniques to demonstrate negative cooperativity with cyclin binding. This cooperative relationship continues to hold promise as an underexplored mechanism of CDK2 inhibition, only observed with ANS prior<sup>19</sup>. Furthermore, the challenge of developing selectivity for CDK2 over structurally similar kinases like CDK1 has been overcome, as seen in both biophysical and the appropriate cellular contexts. Finally, we show that mouse testes incubated with our allosteric CDK2 inhibitors recapitulate features of a *Cdk2*<sup>-/-</sup> phenotype.

## Results

### Anthranilic acids as allosteric CDK2 inhibitors

As described in detail elsewhere, we discovered that anthranilic acids bind the ANS allosteric pocket of CDK2 using a combination of high-throughput and virtual screening<sup>27</sup>. The first compound crystallized of this series was **1**, which binds CDK2 with low micromolar affinity as measured by isothermal titration calorimetry (ITC) and by surface plasmon resonance (SPR) using the steady-state approximation (SSA) affinity fit (Fig. 1a–f, Supplementary Figs. 1–3, Supplementary Table 1).

The carboxylic acid of **1** forms a charge-charge interaction with the side chain of the catalytic residue K33 in the hydrophobic interior of the protein, the same residue that engages the sulfonic acid in ANS (Fig. 1a–c, Supplementary Figs. 1–2). Due to the strength of this type of interaction in a nonpolar environment, it is likely crucial for the binding of these allosteric inhibitors. In addition, the carboxylic acid is held in place through polar interaction with the backbone N-H of F146 of the DFG motif (Supplementary Fig. 2). The N-H of the indole forms a hydrogen bond interaction with the backbone carbonyl of L58 of the C-helix, and the remainder of the binding interaction seem to be driven by van der Waals forces in a pocket largely composed of hydrophobic residues. Both **1** and ANS are amphipathic in nature, with a negatively charged moiety driving the binding to K33 and much of the remaining structure engaging with the hydrophobic pocket.

We next made two substantial improvements to the anthranilic acid series. First, we sought to replace the nitro group on the benzene ring, as this group can be toxic in biological systems<sup>28</sup>. We find the trifluoromethyl group in **2** not only improves the affinity 2-fold but retains a strong enthalpic contribution of binding with a lesser entropic penalty (Fig. 1d, Table 1, Supplementary Fig. 4). The binding pose of **2** to CDK2 is nearly identical to that of **1** (PDB ID 7S84, Supplementary Figs. 1–2, Supplementary Table 1). To confirm the allosteric nature of this series, we analyzed the affinity of **2** in the presence of CDK2 ATP-site inhibitors roscovitine and dinaciclib via ITC, finding the affinity of **2** largely unchanged and providing evidence that binding by our allosteric inhibitors does not substantially affect ATP-site ligand binding (Supplementary Fig. 5). To substantiate this notion, we determined cocrystal structures of CDK2 liganded with **1** and dinaciclib or **1** and roscovitine, demonstrating the ability of CDK2 to form ternary complexes with type III (compound **1**) and type I inhibitors (Fig. 1g,h). Next, substitutions at the 6 position of the indole improve the affinity substantially. Linear groups like nitrile (**3**) or larger halogens like chlorine (**4**) or bromine (**5**) at this position afford binding with less enthalpic benefit and greater entropic contribution (Fig. 1d, Table 1, Supplementary Fig. 4). The nitrile group at this position on the indole in **3** may linearize the molecule compared to **2** and subsequently increase its solvation shell, which is broken when bound into the allosteric pocket. The increased hydrophobicity of **4** and **5** take this principle further, as binding of these compounds into the hydrophobic allosteric pocket led to a greater entropy increase. We were able to orthogonally confirm the affinities of many of these compounds with nanomolar affinities by SPR (Supplementary Fig. 6).

### Relationship of allosteric inhibitors with cyclin binding

To explore the inhibitory potential of these compounds, **4** and **5** were selected for further biophysical testing. Despite its high affinity for CDK2, **4** poorly inhibits a variety of CDK/cyclin complexes in commercial kinase activity assays (Supplementary Table 2). Further analysis of the crystal structure of **1** bound to CDK2 reveals that the allosteric inhibitor engages with L53 and L58 of the C-helix, potentially in a manner incompatible with cyclin A binding that would require a reorientation of the C-helix (Fig. 1a–c). It is likely that in this CDK panel, in which tight-binding cyclin is preincubated with each respective CDK enzyme, the binding of **4** is precluded by the CDK/cyclin PPI (i.e., the CDK2/cyclin A/AI/E/O complexes).

To test this hypothesis, we took advantage of an intramolecular Förster Resonance Energy Transfer (FRET) assay developed to indirectly track the position of the activation loop on CDK2 and thus various conformational states of the kinase. In this assay, CDK2 is modified by attaching an Alexa Fluor® donor/acceptor dye pair split between a relatively stable region of the kinase and the mobile activation loop<sup>29</sup>. As cyclin A is titrated into CDK2 and the activation loop is stabilized in its active outward conformation, the donor:acceptor ratio of the dyes increases (Fig. 2a). In the absence of cyclin, when **4** and **5** are titrated into this CDK2 system, the donor:acceptor ratio shifts to a

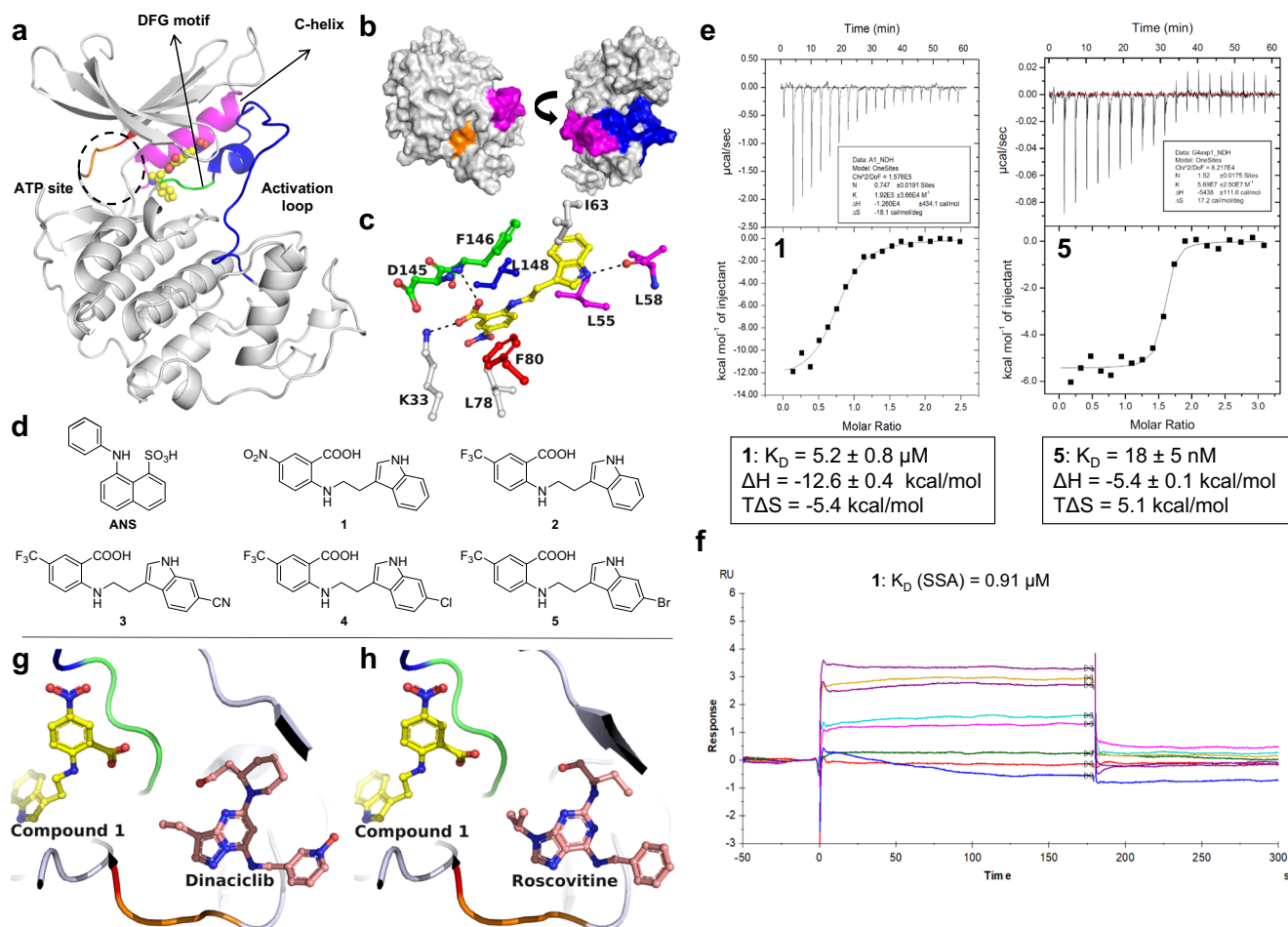


**Fig. 1 | Binding characterization of anthranilic acids as CDK2 allosteric inhibitors.** **a** Co-crystal structure of **1** (yellow) bound to an allosteric pocket of CDK2 (PDB ID 7RWF). The C-helix is shown in magenta, the activation loop in blue, the DFG motif in green, the hinge region in orange, and the gatekeeper residue F80 in red. **b** Surface presentation of the compound **1**-CDK2 complex in two orientations. Compound **1** is buried and largely shielded from solvent. **c** Detailed view of the binding site and interacting residues. H-bonds ( $d = 2.2\text{--}3.5 \text{ \AA}$ ) are indicated as black

dotted lines. Hydrophobic van-der-Waals interactions ( $d = 3.3\text{--}4.0 \text{ \AA}$ ) were omitted for clarity. **d** Chemical structures of CDK2 allosteric inhibitors. **e** ITC traces and thermodynamic binding values of **1** (left) and **5** (right). **f** One of two independent SPR replicates in Supplementary Fig. 3. **g** Co-crystal structure of CDK2 with compound **1** and dinaciclib (pink, PDB ID 8FOW). **h** Co-crystal structure of CDK2 with compound **1** and roscovitine (pink, PDB ID 8FP0). **g** and **h** Demonstrate the non-competitive, allosteric nature of compound **1**.

lower value without fluorescence interference from these small molecule inhibitors, representing a different ensemble of inactive state(s) of CDK2 with corresponding  $K_D$  values of 280 nM and 200 nM, respectively (Fig. 2b, Supplementary Figs. 7–8). However, as the cyclin A concentration is increased, the affinities of both small molecules decrease. For example, a cyclin A concentration of  $1.9 \mu\text{M}$  increases the  $K_D$  of compound **5** to  $1.5 \mu\text{M}$ , a change of nearly tenfold (Fig. 2b). This change in affinity is even more pronounced for compound **4** (Supplementary Fig. 7) and supports the negative cooperative relationship with cyclin binding that was hypothesized by structural analysis.

**Table 1 | Enthalpic and entropic contributions of binding by each ligand and their respective affinity, as determined by ITC**

Compound	$n$ (binding stoichiometry)	$\Delta H$ (kcal/mol)	$\Delta S$ (kcal/mol)	$K_D$ (nM)
<b>1</b>	0.747	-13	-5.4	5200
<b>2</b>	1.03	-9.4	-1.7	2300
<b>3</b>	1.27	-7.9	2.5	23
<b>4</b>	1.39	-5.5	4.8	31
<b>5</b>	1.52	-5.4	5.1	18

Next, we wanted to examine if this negative cooperativity is also observed in a CDK2 ADP Glo activity assay. We tested **5** rather than **4** due to its stronger affinity observed in the FRET experiments in the presence of cyclin A. Because traditional activity assays where the CDK2/cyclin complex is preformed do not demonstrate inhibition with our allosteric CDK2 inhibitors, we preincubated p-CDK2 with our allosteric inhibitor before adding varying amounts of cyclin A. At a 1:1 p-CDK2:cyclin molar ratio, the  $IC_{50}$  of **5** is ~8-fold more potent than at a 1:10 ratio and >100-fold more potent than at a 1:100 ratio, showing a negative cooperative relationship with cyclin (Fig. 2c,d). The negative cooperativity observed in this kinase activity assay agrees with the conformational FRET assay (Fig. 2b). In contrast, the potency of ATP-site inhibitor dinaciclib is largely independent of cyclin concentration (Fig. 2d, Supplementary Fig. 9). To understand why the order of allosteric inhibitor and cyclin addition is important, we returned to the SPR assay to compare the binding kinetics of both our inhibitors and cyclin toward CDK2. As seen with previous CDK2 inhibitors, our allosteric inhibitors exhibit a fast association and fast dissociation rate (Fig. 2e, Supplementary Fig. 2, Supplementary Fig. 6)<sup>30</sup>. In contrast, cyclin has a similarly high affinity ( $K_D = 3.1 \text{ nM}$  and  $K_D = 2.6 \text{ nM}$ , from two independent replicates) but also has a 10+ -fold slower dissociation rate compared to the allosteric inhibitors tested (Fig. 2e,f, Supplementary Fig. 6, Supplementary Fig. 10). Therefore, when cyclin A

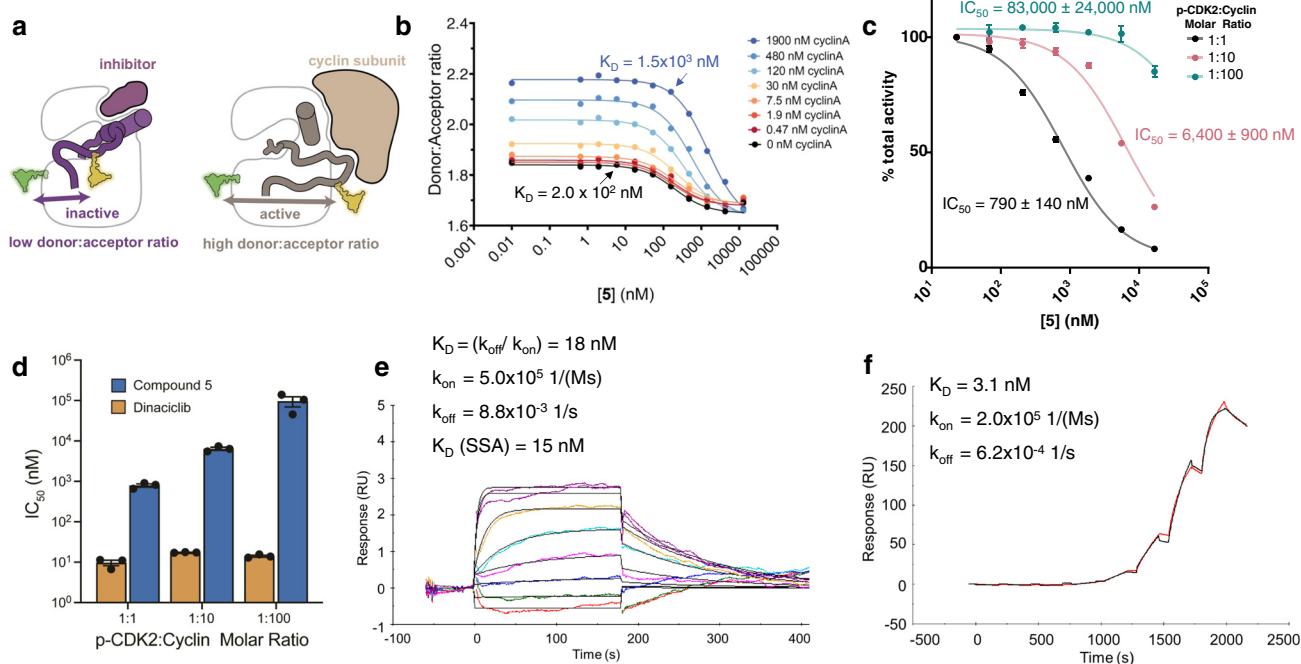


**Fig. 2 | Compound 5 demonstrates negative cooperativity with cyclin A.** **a** An intramolecular FRET assay was developed for CDK2 to track the position of the activation loop. **b** Compound **5** has lower affinity for CDK2 in the FRET assay as cyclin concentration increases. **c** As cyclin concentration increases in an activity assay, the inhibitory potential of **5** decreases. Error bars represent SEM for  $n = 3$  independent replicates. **d** The  $IC_{50}$  values of compound **5** compared to ATP-site inhibitor dinaciclib with varying p-CDK2:cyclin ratios from  $n = 3$  independent

replicates. Error bars represent the 95% confidence interval of the fitted  $IC_{50}$  values whereas the center is the best fit value. **e** One of two independent SPR replicates of **5** binding to CDK2 reveals a fast on, fast off binding profile. **f** One of two independent SPR replicates of cyclin binding to CDK2 reveals a slower off rate than that observed for small molecule inhibitors. Source data for (**b–d**) are provided as a Source Data file.

binds to CDK2, its slow dissociation precludes CDK2 from sampling the inactive conformation necessary for our allosteric inhibitors to bind. In contrast, the fast dissociation of the allosteric inhibitors allows cyclin to bind monomeric CDK2 and trap it in an active conformation, which is more pronounced as cyclin concentrations increase.

### Relationship of allosteric inhibitors with ATP

After exploring the negatively cooperative relationship between cyclin and our allosteric inhibitors, we next examined the effect of ATP on the activity of our allosteric inhibitors. Interestingly, both compound **5** and dinaciclib show lower inhibitory potential with increasing concentrations of ATP (Fig. 3a–c). While this result is expected for dinaciclib, which competes with ATP by binding at the same site, it was surprising considering the noncompetitive nature between ATP-site inhibitors and our allosteric inhibitors observed in monomeric CDK2 without cyclin bound (Fig. 1g,h, Supplementary Fig. 5). Notably, relatively high concentrations of ATP were used for these experiments, ranging from 3+ - to 30+ -fold higher than the reported  $K_m$  of ATP toward CDK2/cyclin A complexes<sup>31</sup>.

Attempts to obtain a cocrystal structure of monomeric CDK2 liganded with **1** and Mg-ATP failed, and different ratios of Mg-ATP and **1** resulted in binary complexes with either **1** or Mg-ATP bound. Comparison of the ATP site between the different complexes reveals that the DFG motif adopts a conformation in the CDK2/Mg-ATP complex that is incompatible for the interaction with **1** (Fig. 3d–f). This DFG conformation is held in place tightly through direct interaction of the side chain of D145 with the  $Mg^{2+}$  ion coordinating the triphosphate oxygens of ATP. Binding of **1** requires the DFG main chain to shift by ~2 Å toward the ATP site, imposing steric clashes on Mg-ATP and causing a mutually exclusive interaction between Mg-ATP and **1**. For type I inhibitors such as dinaciclib and roscovitine, the DFG motif is not engaged in critical binding interactions, and the DFG backbone is free

to adopt a conformation compatible with the concomitant binding of **1**.

### Selectivity of allosteric inhibitors

To explore the selectivity of these compounds, we next assessed target engagement in a cellular thermal shift assay (CETSA)<sup>32</sup>. Jurkat cells were selected for CETSA due to prior work showing a predictable  $T_{agg}$  across multiple, independent DMSO control experiments for CDK1 and CDK2 in this cell line<sup>33</sup>. In addition, Jurkat cells do not express a high amount of A- and E-type cyclins (Human Protein Atlas proteinatlas.org)<sup>34</sup>, making it possible to observe binding of our compounds to free, noncomplexed CDK2. Compound **5** is cell permeable, as shown by the intracellular engagement and thermal stabilization of CDK2 ( $\Delta T_{agg} = 8.3^\circ C$ ). No stabilization of CDK1 is observed ( $\Delta T_{agg} = 0.4^\circ C$ ), suggesting that **5** is selective for CDK2 over the very similar CDK1 in this cellular context (Fig. 4a, Supplementary Fig. 11).

We sought to confirm the selectivity observed in the CETSA more directly in an orthogonal assay. Previous examination of ATP-site inhibitor dinaciclib under similar SPR conditions revealed a  $K_D$  (SSA) =  $78 \pm 16$  nM for CDK2 and a  $K_D$  (SSA) =  $1.8 \pm 0.2$   $\mu M$  for CDK1 ( $K_D = \text{mean} \pm \text{standard deviation}$  from two independent repeats)<sup>30</sup>. In contrast, we find compound **5** does not bind CDK1 while it binds CDK2 with a  $K_D$  (SSA) = 15 nM and  $K_D$  (SSA) = 17 nM (Fig. 2e, Supplementary Fig. 6, Supplementary Fig. 12,  $K_D$  values from two independent repeats). We confirmed the validity of our CDK1 protein by testing dinaciclib, which binds CDK1 similarly to what was discovered previously with a  $K_D$  (SSA) = 1.2  $\mu M$  and  $K_D$  (SSA) = 1.8  $\mu M$  (Supplementary Fig. 12,  $K_D$  values from two independent repeats). Therefore, both the CETSA and SPR data suggest that allosteric inhibitor **5** has exquisite selectivity for CDK2 over CDK1. In addition, a kinome screen of compound **5** did not show >80% inhibition of any kinase at a 10  $\mu M$  concentration, and only 4% of the 371 kinases tested showed >50%

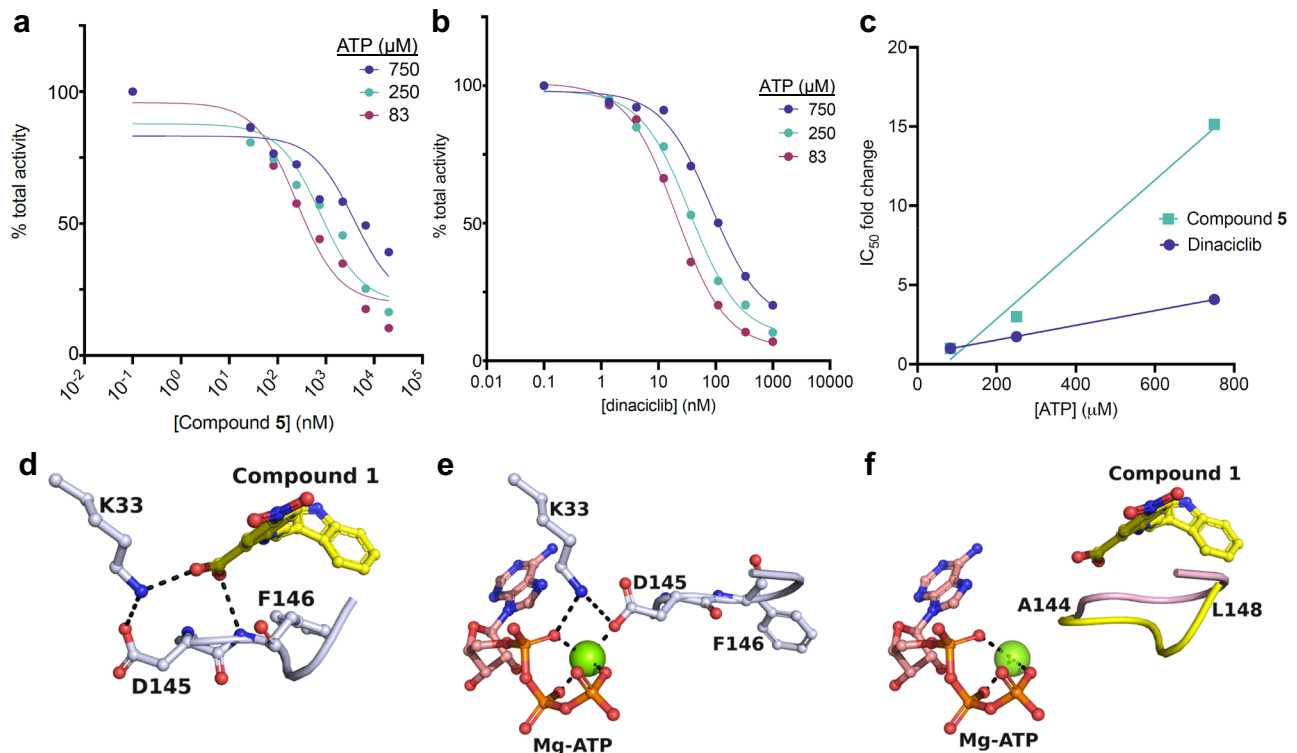


**Fig. 3 | Allosteric CDK2 inhibitors are incompatible with ATP binding.** Both compound 5 (a) and dinaciclib (b) show a lower inhibitory potential of CDK2 with increasing concentrations of ATP, as quantified and compared in (c). One replicate was performed for the experiments with compound 5 while two technical replicates were performed for the experiments with dinaciclib and data points plotted in (b) represent the mean values. Source data for (a–c) are provided as a Source Data file.

The DFG motif around D145 in the CDK2-compound 1 complex (d) adopts a different conformation in the CDK2-ATP complex (e, PDB ID 8FP5). f Superposition of the two complexes reveals that the backbone around the DFG motif (pink for CDK2-ATP, yellow for CDK2-compound 1) shifts by about 2 Å upon interaction with compound 1.

inhibition (Supplementary Table 3). This selectivity is significant, as many other previously developed and clinically tested ATP-site CDK2 inhibitors like dinaciclib demonstrate off-target toxicity due to their inability to differentiate between these two kinases<sup>30,35,36</sup>. With this promising feature of our allosteric inhibitors, we next sought to confirm if the negative cooperativity between 5 and cyclin previously observed in the biophysical assays also translates to a cellular context.

### Biological testing of allosteric inhibitors

To further examine the negatively cooperative relationship found in biophysical studies, we examined the target engagement of 5 in cancer cells driven by cyclin overexpression. We chose the ovarian cancer cell line OVCAR-3, where prior work has established via in vitro and in vivo genetic knockdown experiments that growth of OVCAR-3 cells is driven by cyclin E1 overexpression and dependent on CDK2. In addition, as a demonstration of the dependence on CDK2, dinaciclib has previously shown significant toxicity in OVCAR-3 cells<sup>37</sup>. Despite binding with CDK2 in Jurkat cells, 5 is relatively nontoxic in OVCAR-3 cells driven by cyclin E1 overexpression, in contrast to the positive control staurosporine (Supplementary Fig. 13). To examine engagement with CDK2 in a high cyclin context, we performed similar CETSA experiments in OVCAR-3 cells as was initially done in Jurkat cells. These experiments show that in contrast to the profound stabilization 5 affords CDK2 in Jurkat cells, there is no stabilization of CDK2 by 5 in OVCAR-3 cells (Fig. 4b, Supplementary Fig. 14). This is likely due to the high cyclin content in OVCAR-3 cells, which precludes binding of our compound to the allosteric pocket. We further confirmed the previously reported overexpression of cyclin E1 in OVCAR-3 cells and compared it to expression levels in Jurkat cells, finding a significant 8.5-fold increase in the cyclin E1:CDK2 ratio in OVCAR-3 cells compared to

that in Jurkat cells (Fig. 4c, Supplementary Fig. 15)<sup>37</sup>. Coupling the cellular CETSA data with the negative cooperativity with cyclin A observed in the structural FRET and kinase activity assays, 5 substantially binds CDK2 when cyclins are not overexpressed and can disrupt the interaction between CDK2 and its protein binding partners in these contexts.

To assess the utility of our compounds to disrupt CDK2 protein engagement in non-cyclin overexpressing contexts, their contraceptive potential was next explored. CDK2's meiotic function is controlled via a cyclin-independent mechanism, namely the binding of a distinct activator protein, SPY1<sup>17</sup>. In particular, the CDK2/SPY1 interaction is crucial for homologous chromosomal pairing and synapse formation, double-strand break processing, and facilitating crossing-over in prophase I; both *Cdk2*<sup>-/-</sup> and *Spdy1*<sup>-/-</sup> spermatocytes exhibit a disruption of these events<sup>14,17,38</sup>. Because the crystal structure of SPY1 bound to CDK2 reveals a smaller protein with fewer protein-protein contacts than cyclin proteins, it is feasible that the affinity of this interaction could be weaker than that between CDK2 and cyclin<sup>16</sup>. This would lead to an inhibitor that selectively disrupts CDK2/SPY1 complexes but leaves CDK2/cyclin complexes intact. To assess the contraceptive potential of our compounds, we tested 5 in spermatocyte chromosome spreads from mouse testicular explants, as we knew it was cell permeable and binds to CDK2 when cyclins are not overexpressed. After addition of 5, we examined the chromosomal arrangement by staining for SYCP1/3 as well as the localization of RAD51 and CDK2. Normally, RAD51 localizes to synapses only transiently and therefore is captured by microscopy in asynapsed regions. In contrast, both *Cdk2*<sup>-/-</sup> and *Spdy1*<sup>-/-</sup> spermatocytes arrest meiosis in such a unique fashion that RAD51 can be found localized to synapsed regions<sup>17,38</sup>. Spermatocyte chromosome spreads incubated with 5

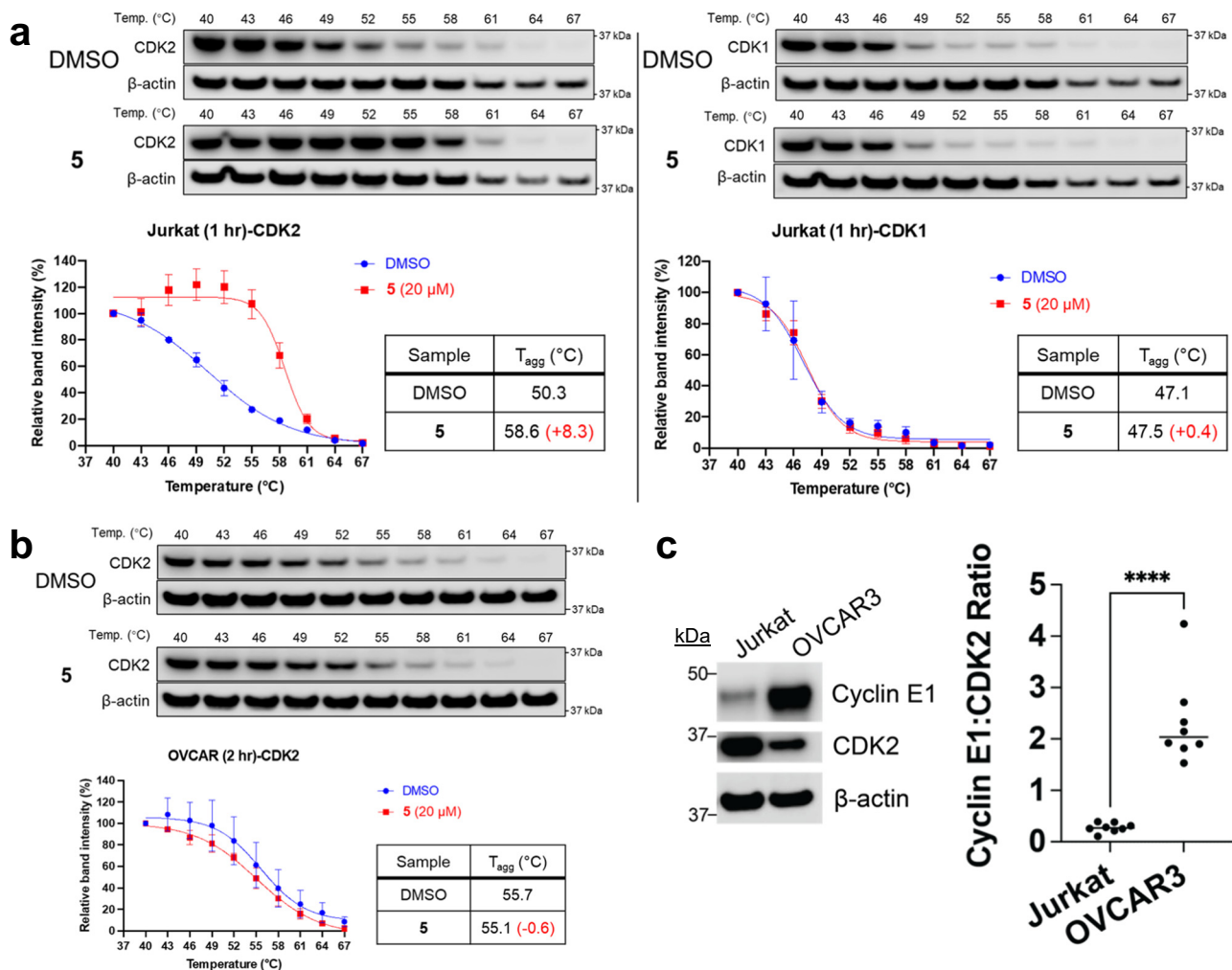


**Fig. 4 | Target engagement of compound 5 as assessed by CETSA. a** Compound 5 stabilizes CDK2 over CDK1 intracellularly in CETSA experiments using Jurkat cells. **b** Compound 5 does not stabilize CDK2 over DMSO control in CETSA experiments using OVCAR-3 cells. Protein abundance curves from the CETSA experiments indicate mean  $\pm$  SEM from  $n = 3$  biological replicates. **c** The cyclin E1:CDK2 ratio is significantly higher in OVCAR3 cells than in Jurkat cells, as shown by a

representative immunoblot of cyclin E1 and CDK2 in Jurkat and OVCAR3 cells as well as by a quantification of immunoblots shown graphically ( $n = 8$  independent replicates for each cell line). An unpaired two-sided student's  $t$  test without adjustments was used to compare the groups, finding  $p = 9.0 \times 10^{-6}$  [\*\*\*\* indicates  $p < 0.0001$ ]. Source data are provided as a Source Data file.

(100 μM, 6 h) show significantly more abnormal RAD51 staining at or near the telomeres in synapsed regions compared to control treated explants, indicating arrested and unrepaired DNA double strand breaks (Fig. 5a,b,  $p = 0.017$ ). In addition, more meiotic cells show abnormal CDK2 staining on chromosomes within the nuclei in the presence of 5 (50% of samples) compared to control samples (17%), indicating disruption of CDK2 meiotic function via improper localization of CDK2 to telomeres, as the microscopic CDK2 signal fades into the cytoplasmic background but robust expression of CDK2 can still be seen by Western blot (Fig. 5c, Supplementary Fig. 16). In contrast, SPY1 telomeric localization was unchanged (Fig. 5c), consistent with prior work supporting SPY1 as localizing to telomeric ends prior to CDK2 and acting as a necessary recruiter of CDK2 to telomeric ends<sup>17,39</sup>. The loss of colocalization of CDK2 and SPY1 at telomeric ends further supports the disruption of the CDK2-SPY1 complex as a probable mechanism for how compound 5 arrests meiosis. Whereas the lack of OVCAR-3 cytotoxicity from 5 suggests that cyclin-dependent CDK2 activity can be relatively unaffected in somatic cells by these inhibitors, the mouse testicular explant data show the promise of this allosteric CDK2 inhibitor series to disrupt CDK2/SPY1-driven meiosis to yield an efficacious yet safe contraceptive agent.

## Discussion

The allosteric CDK2 inhibitors in this work stabilize CDK2 in a unique inactive conformation, as demonstrated by X-ray crystallography. Compared to prior structurally-confirmed allosteric CDK2 inhibitors, the affinity of these compounds is markedly improved, demonstrating a  $K_D$  for CDK2 in the nanomolar range<sup>19</sup>. This makes these inhibitors the strongest binding, structurally confirmed allosteric CDK inhibitors reported. Furthermore, the disruption of CDK2 PPI by these inhibitors is well-characterized by their negative cooperative relationship with cyclin binding and deviates mechanically in comparison to traditional type I inhibitors like dinaciclib. In both biophysical and the appropriate cellular contexts, these compounds show an impressive selectivity for CDK2 over structurally similar CDK1, a quality not possessed by many previously developed CDK2 inhibitors. The therapeutic potential of these compounds is exemplified by incubation in spermatocyte chromosome spreads from mouse testicular explants, where they appear to arrest meiosis by recapitulating a phenotype similar to what is observed in *Cdk2*<sup>-/-</sup> and *Spdy4*<sup>-/-</sup> spermatocytes.

One of the most striking findings of this series is the marked selectivity for CDK2 over CDK1, a protein with 65% overall sequence identity and 89% sequence similarity in the ATP-site where most

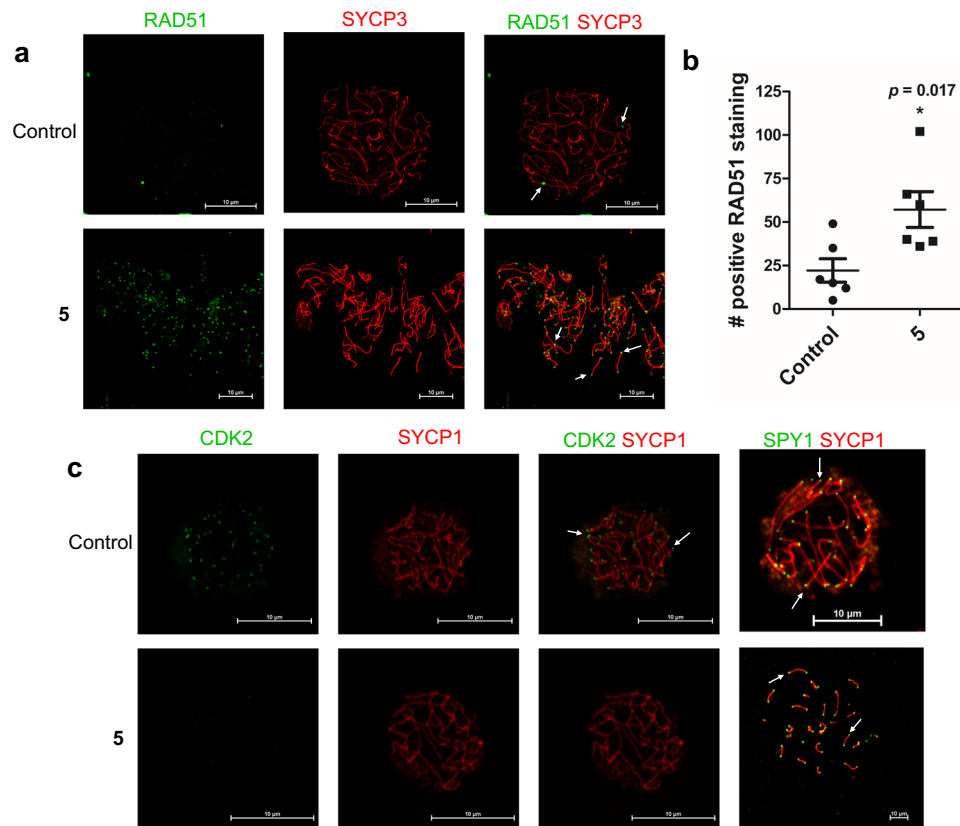


**Fig. 5 | Compound 5 recapitulates features of *Cdk2*<sup>-/-</sup> and *Spdy1*<sup>-/-</sup> phenotypes in spermatocytes. a** RAD51 (green) and SYCP3 (red) are stained in explants treated with either control or **5**. **b** Compound **5** treated samples show significantly more localization of RAD51 at synapsed regions (positive RAD51 staining at telomeres and chromosomes) compared to control. Values graphed are mean  $\pm$  SEM ( $n = 6$  biologically independent samples for each condition). An unpaired two-tail *t*-test was

used to determine the *p*-value without adjustments. **c** CDK2 or SPY1 (green) and SYCP1 (red) are stained in explants treated with either control or **5**. White arrows added to emphasize the altered localization of RAD51/CDK2 and unchanged localization of SPY1 on chromosomes. Source data for (**b**) are provided as a Source Data file.

CDK2 inhibitors bind<sup>40</sup>. Historically, the allure of allosteric kinase inhibitors has been their potential for improved selectivity as compared to traditional ATP-site inhibitors due to less structural similarity at pockets distal to the ATP-site. Interestingly, the residues engaged by the anthranilic acid-derived allosteric inhibitors in this paper are nearly identical between CDK1 and CDK2, and are relatively conserved across the CDK family. For example, the carboxylate of the anthranilic acid binds the catalytic lysine (K33) in CDK2, a residue conserved across kinases. An alternative explanation may be the divergent energy landscapes of inactive kinases. Prior work suggests that despite the structural similarity between CDK2 and CDK1, the energy landscapes of these kinases without cyclin bound differ greatly compared to their respective cyclin-bound states<sup>30</sup>. Because we optimized our ligands to bind an inactive, non-cyclin bound state of CDK2, we observe selectivity in the Jurkat cell CETSA and SPR experiments, where our compounds bind CDK2 but not CDK1. While the ligand-bound inactive states of CDK2 and CDK1 are likely nearly identical due to the structural similarity of these kinases, the binding of these ligands may be biased toward CDK2 over CDK1 due to CDK2's propensity to sample this inactive state or an enhanced flexibility to accommodate allosteric ligand binding, although the precise mechanism remains to be determined. This latter explanation would be consistent with the large degree of conformational sampling observed for inactive, monomeric CDK2<sup>29</sup>. In addition, it has been inferred that inactive CDK1 is more stable than inactive CDK2 and binds cyclin A less readily as a result<sup>41</sup>. The exquisite selectivity of this series beyond CDK1 is further supported by the kinome screen where compound **5** did not significantly inhibit

any kinase >80% and only inhibited a handful of kinases >50% at the high concentration of 10  $\mu$ M.

Whereas most previously developed ATP-site inhibitors are often positively cooperative with cyclin and bind the CDK2/cyclin complex, our allosteric inhibitors are negatively cooperative with cyclin<sup>29</sup>. This is confirmed by the structural FRET assay, where the  $K_D$  of compound **5** toward CDK2 weakens as more cyclin A is added, and by the kinase activity assay, where the  $IC_{50}$  shows less potency as the p-CDK2:cyclin molar ratio decreases. Furthermore, CETSA data with **5** shows stabilization of CDK2 in Jurkat cells, where cyclins are not overexpressed, but not in OVCAR-3 cells, where cyclin E1 drives cell proliferation and survival. While our compounds are not cytotoxic in cyclin overexpressing cancer contexts, disruption of the CDK2/cyclin PPI remains a viable anticancer strategy. Recent work has shown that the complex natural product homoharringtonine (HHT) disrupts the PPI between CDK2 and cyclin A to act as an efficacious anticancer agent, although the allosteric binding mode of HHT has not been experimentally confirmed outside of computational models and its selectivity amongst kinases not explored<sup>42</sup>. In addition, disrupting the CDK2/cyclin interaction may be less toxic than traditional ATP-site inhibitors that sequester cyclin via their positive cooperativity with cyclin binding<sup>15</sup>. Further development of our allosteric inhibitors might confer an advantage in this regard compared to other promising compounds, such as recently developed CDK2/cyclin E1 inhibitor PF-07104091, a selective ATP-site inhibitor targeting the cyclin-bound activated state of the kinase<sup>43</sup>. Future iterations of our allosteric inhibitors with improved affinity and slower off-rates may very well be selective and efficacious in inhibiting a CDK2/cyclin-driven disease

state. Similar success was recently found with allosteric EGFR inhibitors optimized to overcome undesirable EGFR homodimerization, analogous to our goal of overcoming the strength of CDK2/cyclin heterodimerization by increasing the interaction strength between our allosteric inhibitor and CDK2<sup>3–5</sup>. In addition, the observed compatibility of our allosteric inhibitors with type I inhibitors (but not ATP) demonstrates the potential for higher efficacy if type I and our type III CDK2 inhibitors were administered in combination.

Compound **5** potentially affects meiotic CDK2 function, most likely by interfering with SPY1 binding, although the exact mechanism of meiotic disruption by **5** is yet to be confirmed. Prior work has shown that when the scaffolding and catalytic functions of the CDK2/SPY1 complex are disrupted, prophase I is arrested<sup>17</sup>. Our inhibitors similarly arrest prophase I, as evidenced by the significantly increased localization of double-strand break repair protein RAD51 on synapses. In addition, spermatocytes from testis explants treated with **5** show more abnormal CDK2 localization compared to the control while retention of SPY1 localization to telomeric ends. While our compounds arrest meiosis, their potential as effective but safe non-hormonal contraceptive agents requires further exploration. If our hypothesis that these allosteric inhibitors selectively disrupt the meiotic CDK2/SPY1 PPI while leaving the mitotic CDK2/cyclin PPI intact is true, they would be a rare example of PPI inhibitors that derive selectivity by exploiting the different affinities of protein binding partners engaging at the same binding site. Aside from the impact of this work on CDK2 inhibitor development, we hope as the conformational landscapes of other kinases are further elucidated and more allosteric pockets are discovered, this work can serve as a model for allosteric inhibitor development to target other therapeutically important kinases.

## Methods

### Materials

Dinaciclib was purchased from Cayman Chemicals with >98% purity and roscovitine from Selleck Chemicals with >99% purity. The production and purity assessment (>95%) of GST-CDK1 was made possible via NIH HHSN275201800071. The purity of compounds **1–5** were determined to be >95% pure by qNMR<sup>44,45</sup> and described further in the Supplementary Information.

### Research animals

The Animal Care and Use Proposal (ACUP) ACUP Number: 2019 -2508 has been reviewed and approved by the University of Kansas Institutional Animal Care and Use Committee.

### CDK2 and cyclin A protein expression and purification

The gene encoding human CDK2 (1-298) was custom-synthesized (GenScript), subcloned into pGEX6P1 vector providing an N-terminal GST-tag and expressed in *E. coli* BL21 DE3 RIPL cells. Cells were grown at 37 °C for 3 h to OD<sub>600</sub> = 0.6, then grown further until OD<sub>600</sub> = 0.9 at 16 °C, induced with 0.5 mM IPTG and allowed to grow further overnight. Cells were harvested by centrifugation at 6000 × *g* for 20 min, the lysate was subjected to GST-affinity chromatography (GE Life Sciences), the GST tag was removed by PreScission protease, and cleaved CDK2 was subjected to a second GST-affinity chromatography step as described previously<sup>46</sup>. Flow-through fractions containing CDK2 were combined, concentrated and further purified by size exclusion chromatography using a Superdex 75 26/60 column (GE Life Sciences) in 50 mM HEPES, pH 7.5, 150 mM NaCl, 10 mM MgCl<sub>2</sub>, 1 mM EGTA, 0.01 mM ADP, 2 mM DTT. For ITC experiments, purified CDK2 was concentrated to 50–100 μM and flash frozen in appropriate ITC volume aliquots for –80 °C storage.

Expression and purification of p-CDK2 and cyclin A have been described previously<sup>29</sup>. Briefly, to generate CDK2 phosphorylated on T160 (p-CDK2), a 6His-TEV-CDK2 construct (pCDFduet) was coexpressed with yeast CAK (pGEX) overnight in Terrific broth at 18 °C.

Cells were harvested by centrifugation at 5000 × *g* for 20 min and lysed by homogenization (Avestin Emulsiflex C3). Lysates were cleared by centrifugation at 20,000 × *g* for 1 h, subjected to Ni purification (GE HisTrap HP), and p-CDK2 was eluted with 1× PBS, 500 mM imidazole, 10% glycerol. Imidazole was removed by desalting the sample into 1× PBS, 10% glycerol (GE HiPrep 26/10), and the 6His tag was cleaved overnight with TEV protease. The protein was further purified by size exclusion chromatography (GE Superdex S75 10/300 GL), flash frozen and stored at –80 °C.

Bovine cyclin A (171-432 with a C-terminal 6His tag) was expressed overnight in BL21(DE3)pLysS in Terrific broth at 20 °C. Cells were lysed and lysates cleared as above, and the protein was isolated through Ni purification into 50 mM Tris pH 8.25, 300 mM NaCl, 100 mM MgCl<sub>2</sub>, 10% glycerol using a 0–500 mM imidazole gradient. Cyclin A was further purified by size exclusion chromatography (GE Superdex 200 16/600) into 50 mM Tris pH 8.25, 100 mM MgCl<sub>2</sub>, 5 mM 2-mercaptoethanol.

### Crystallization

Purified CDK2 was buffer exchanged into 100 mM Na/K phosphate, pH 6.2, 2 mM DTT using PD10 columns (GE Life Sciences) and concentrated to 9 mg/mL. The CDK2/compound **1** complex was obtained by co-crystallization (15% (v/v) Jeffamine ED2001, 50 mM HEPES, pH 7.5, 4.5 mg/mL CDK2, 5 mM **1**) at 19 °C. The structures of CDK2 with compound **1** and dinaciclib, compound **1** and roscovitine, MgATP, and compound **2** were obtained by in-diffusion of apo CDK2 crystals with the ligands (1–5 mM) at 19 °C for 24 h (10% (v/v) PEG 3350, 50 mM HEPES, pH 7.5, 10% (v/v) ethylene glycol, 4.5 mg/mL CDK2).

### Data collection and refinement

X-ray diffraction data of CDK2 liganded with compound **1** or Mg-ATP were collected on a Rigaku Micro-Max 007-HF X-ray generator, equipped with a CCD Saturn 944 system located in the Chemical Biology Core of the Moffitt Cancer Center. Data of CDK2 liganded with compound **2**, compound **1** and dinaciclib, compound **1** and roscovitine were collected at the GM/CA beamline (23ID-B with Dectris PILATUS 3-6 M detector, 23ID-D with Dectris EIGER 16 M detector) at Argonne National Laboratory. All data were collected at 93 K, processed and scaled with XDS<sup>47</sup>. The structures were solved by molecular replacement using PDB 4KD1 as the start model in PHASER<sup>48</sup>. Ligand geometrical restraints were generated with Phenix Elbow<sup>49</sup>. All structures were refined with Phenix<sup>50</sup>, and model building was performed with Coot<sup>51</sup>. Data collection and refinement statistics are shown in Supplementary Table 1.

### Compound synthesis and characterization

The NMR spectra and HRMS data for the compounds described below are shown in Supplementary Figs. 17–21. The qNMR purity assessment is also included in the Supplementary Information.

General method of S<sub>n</sub>Ar followed by hydrolysis to yield anthranilic acids **1–5**: Commercial methyl 2-bromo or 2-fluoro-5-(nitro) or 5-(trifluoromethyl)benzoates (0.30 mmol) were dissolved in DMF (5 mL) with 1.1 equivalents of commercial tryptamine derivatives (in their neutral form or as HCl salts) and sodium bicarbonate (3–4 equiv). An exception was that for **3**, the synthesis of the nitrile tryptamine precursor was accomplished using a previously described method<sup>52</sup>. The reaction temperature employed was room temperature for compound **1** and 70 °C for compounds **2–5**. The solution was stirred for 12 h. After, 1 M HCl (aq) was added until pH <7 the solution was extracted into DCM (2×). The DCM solvent was removed via rotary evaporation and the crude product was dissolved in MeOH to proceed to the hydrolysis step without purification. Water was added to the MeOH mixture until a 1:1 ratio of solvents was reached. A solution of 5 M NaOH (aq) (1 mL) was added, and the hydrolysis proceeded at 50 °C for 12 h and was monitored by TLC for completion. The mixture was cooled to room



temperature and the solvent was removed by rotary evaporation. 1 M HCl (aq) was added until pH < 4 and then the solution was extracted into EtOAc (2×). The EtOAc layer was dried with MgSO<sub>4</sub> and loaded onto Celite. Subsequent purification was accomplished by silica gel flash column chromatography with a gradient of EtOAc in hexanes of 0–100% over 7 min, eluting around 60% EtOAc as the free carboxylic acid. The solvent was removed by rotary evaporation and the acid was isolated as the final product.

2-((1*H*-Indol-3-yl)ethyl)amino)-5-nitrobenzoic Acid (**1**). 78% yield. Yellow solid. m.p. 216–218 °C. <sup>1</sup>H NMR (400 MHz, DMSO-*d*<sub>6</sub>) δ 13.35 (s, 1H), 10.90 (s, 1H), 8.85 (s, 1H), 8.63 (s, 1H), 8.16 (d, *J* = 9.3 Hz, 1H), 7.60 (d, *J* = 7.8 Hz, 1H), 7.35 (d, *J* = 8.1 Hz, 1H), 7.25 (s, 1H), 7.08 (t, *J* = 7.5 Hz, 1H), 6.99 (t, *J* = 7.4 Hz, 1H), 6.93 (d, *J* = 9.6 Hz, 1H), 3.64 (q, *J* = 6.9 Hz, 2H), 3.07 (t, *J* = 7.0 Hz, 2H). <sup>13</sup>C NMR (101 MHz, DMSO-*d*<sub>6</sub>) δ 168.6, 154.5, 136.3, 134.5, 129.5, 128.6, 127.0, 123.3, 121.1, 118.4, 118.3, 111.7, 111.4, 110.9, 109.0, 43.0, 24.3. HRMS (*m/z*): [M]<sup>-</sup> calcd. for C<sub>17</sub>H<sub>15</sub>N<sub>3</sub>O<sub>4</sub>, 324.0990; found, 324.0985.

2-((1*H*-Indol-3-yl)ethyl)amino)-5-(trifluoromethyl)benzoic Acid (**2**). 33% yield. Light yellow solid. m.p. 201–202 °C. <sup>1</sup>H NMR (400 MHz, DMSO-*d*<sub>6</sub>) δ 13.05 (s, 1H), 10.88 (s, 1H), 8.34 (s, 1H), 8.02 (s, 1H), 7.63 (d, *J* = 9.0 Hz, 1H), 7.59 (d, *J* = 7.9 Hz, 1H), 7.35 (d, *J* = 8.1 Hz, 1H), 7.23 (s, 1H), 7.08 (t, *J* = 8.2 Hz, 1H), 7.01–6.92 (m, 2H), 3.55 (t, *J* = 7.2 Hz, 2H), 3.05 (t, *J* = 7.0 Hz, 2H). <sup>13</sup>C NMR (151 MHz, DMSO-*d*<sub>6</sub>) δ 168.8, 152.6, 136.2, 130.6, 128.7, 126.9, 124.6 (q, *J* = 270.3 Hz), 123.0, 120.9, 118.18, 118.18, 113.8 (q, *J* = 32.5 Hz), 111.8, 111.3, 111.0, 109.1, 42.6, 24.2. HRMS (*m/z*): [M]<sup>-</sup> calcd. for C<sub>18</sub>H<sub>15</sub>F<sub>3</sub>N<sub>2</sub>O<sub>2</sub>, 347.1013; found, 347.1006.

2-((2-(6-Cyano-1*H*-indol-3-yl)ethyl)amino)-5-(trifluoromethyl)benzoic Acid (**3**). 9% yield over 5 steps<sup>52</sup>. Colorless solid. m.p. 190–191 °C. <sup>1</sup>H NMR (400 MHz, DMSO-*d*<sub>6</sub>) δ 13.13–13.08 (m, 1H), 11.50 (s, 1H), 8.37 (s, 1H), 8.01 (s, 1H), 7.85 (s, 1H), 7.78 (d, *J* = 8.2 Hz, 1H), 7.63 (dd, *J* = 8.9, 2.4 Hz, 1H), 7.57 (s, 1H), 7.32 (dd, *J* = 8.2, 1.5 Hz, 1H), 6.96 (d, *J* = 9.0 Hz, 1H), 3.56 (t, *J* = 7.0 Hz, 2H), 3.07 (t, *J* = 7.0 Hz, 2H). <sup>13</sup>C NMR (151 MHz, DMSO-*d*<sub>6</sub>) δ 169.0, 152.7, 135.0, 130.7, 130.2, 128.9, 128.0, 124.8 (q, *J* = 270.3 Hz), 121.0, 120.8, 119.6, 116.3, 114.0 (q, *J* = 32.5 Hz), 112.5, 112.0, 109.3, 102.3, 42.7, 24.0. HRMS (*m/z*): [M]<sup>-</sup> calcd. for C<sub>19</sub>H<sub>14</sub>F<sub>3</sub>N<sub>3</sub>O<sub>2</sub>, 372.0965; found, 372.0959.

2-((2-(6-Chloro-1*H*-indol-3-yl)ethyl)amino)-5-(trifluoromethyl)benzoic Acid (**4**). 70% yield. Colorless solid. m.p. 207–210 °C. <sup>1</sup>H NMR (400 MHz, DMSO-*d*<sub>6</sub>) δ 13.09 (s, 1H), 11.03 (s, 1H), 8.33 (s, 1H), 8.01 (s, 1H), 7.67–7.57 (m, 2H), 7.39 (s, 1H), 7.29 (s, 1H), 6.99 (dd, *J* = 8.4, 1.9 Hz, 1H), 6.96 (d, *J* = 9.0 Hz, 1H), 3.57–3.53 (m, 2H), 3.03 (t, *J* = 7.0 Hz, 2H). <sup>13</sup>C NMR (151 MHz, DMSO-*d*<sub>6</sub>) δ 168.9, 152.7, 136.6, 130.7, 128.8, 125.9, 125.8, 124.7 (q, *J* = 270.3 Hz), 124.3, 119.8, 118.6, 113.9 (q, *J* = 32.6 Hz), 111.9, 111.6, 111.0, 109.2, 42.7, 24.2. HRMS (*m/z*): [M]<sup>-</sup> calcd. for C<sub>18</sub>H<sub>14</sub>ClF<sub>3</sub>N<sub>2</sub>O<sub>2</sub>, 381.0623; found, 381.0637.

2-((2-(6-Bromo-1*H*-indol-3-yl)ethyl)amino)-5-(trifluoromethyl)benzoic Acid (**5**). 44% yield. Colorless solid. m.p. 213–214 °C. <sup>1</sup>H NMR (400 MHz, DMSO-*d*<sub>6</sub>) δ 13.10 (s, 1H), 11.04 (s, 1H), 8.33 (s, 1H), 8.01 (s, 1H), 7.63 (d, *J* = 8.9 Hz, 1H), 7.60–7.51 (m, 1H), 7.28 (s, 1H), 7.11 (d, *J* = 8.4 Hz, 1H), 6.96 (d, *J* = 9.0 Hz, 1H), 3.57–3.52 (m, 2H), 3.03 (t, *J* = 7.1 Hz, 2H). <sup>13</sup>C NMR (151 MHz, DMSO-*d*<sub>6</sub>) δ 169.0, 152.7, 137.1, 130.7, 128.9, 126.2, 125.7, 124.3, 123.9, 121.2, 120.2, 113.9, 113.8, 111.9, 111.7, 109.3, 42.7, 24.2. HRMS (*m/z*): [M]<sup>-</sup> calcd. for C<sub>18</sub>H<sub>14</sub>BrF<sub>3</sub>N<sub>2</sub>O<sub>2</sub>, 425.0118; found, 425.0133.

### Isothermal titration calorimetry (ITC)

CDK2 was thawed at room temperature and the buffer was exchanged using Zeba™ spin desalting columns. The final ITC buffer was 1× PBS, 10 mM MgCl<sub>2</sub>, and 5% glycerol (pH = 7.4), with 5% DMSO added after buffer exchange into the protein solution and from a 1:20 concentrated DMSO stock for the ligand solution. CDK2 concentration was determined using a NanoDrop™ spectrophotometer and calculated using absorption at 280 nm ( $\epsilon = 36,900 \text{ M}^{-1} \text{ cm}^{-1}$ ). Into a 96-well plate for automatic injection for the MicroCal iTC200 (Malvern), a final volume of 400  $\mu\text{L}$  protein solution for the sample cell and 200  $\mu\text{L}$

inhibitor solution for the injecting syringe were placed into the appropriate wells. The final inhibitor concentration in the syringe was 500–1000  $\mu\text{M}$  depending on compound solubility. For experiments with compound **2** in the presence of ATP-site inhibitors roscovitine or dinaciclib, 100  $\mu\text{M}$  ATP-site inhibitor was present in both the syringe and sample cell. For compounds **3–5**, to get more accurate data on the ITC with appropriate *c* values<sup>33</sup>, the CDK2 concentration was lowered -10-fold to 5  $\mu\text{M}$  and the syringe concentration lowered to 75  $\mu\text{M}$ . The ITC experiments were conducted at 25 °C and 750 rpm stirring, with a discarded initial 0.4  $\mu\text{L}$  injection and 20 subsequent 4  $\mu\text{L}$  injections with 180 s between injections. A one-site binding model was used to fit the ITC data after adjusting the baseline to account for slight buffer mismatch between the cell and syringe samples.

### Surface plasmon resonance (SPR)

The SPR method used was largely adapted from a published method for CDK1 and CDK2 SPR studies<sup>30</sup>. A Biacore S200 (Cytiva) at 20 °C and CM5 chips were used for binding analysis. Multi-cycle runs were used for small molecule binding analysis, whereas a single-cycle run was used to measure cyclin binding. The buffer used to prepare the protein samples was 20 mM HEPES, 150 mM NaCl, 10 mM MgCl<sub>2</sub>, 0.01% Tween 20, pH = 7.4. For runs with small molecules, an additional 1% DMSO was added for solubility. GST capture kit conditions (Cytiva catalog number BR100223) were used to capture anti-GST antibody on both the sample and reference cells (7 min immobilization, 10  $\mu\text{L}/\text{min}$  flow rate). Both surfaces had high affinity sites capped with an additional 3 min of GST flowed over (5  $\mu\text{g}/\text{mL}$  concentration, 5  $\mu\text{L}/\text{min}$  flow rate) followed by regeneration (10 mM glycine, pH = 2.2). On the subtractive reference surface, GST was immobilized (20  $\mu\text{g}/\text{mL}$ , 5  $\mu\text{L}/\text{min}$ , 5 min). On the sample surface, GST-tagged CDK1 or GST-tagged CDK2 (with the GST cleavage stepped skipped during the purification process) was immobilized in a similar fashion (50  $\mu\text{g}/\text{mL}$ , 5  $\mu\text{L}/\text{min}$ , 5 min). For GST-tagged unphosphorylated CDK1, a filtration through a Fisherbrand™ syringe filter: PTFE Membrane (0.45  $\mu\text{m}$  pore size, 13 mm diameter) was performed to lessen aggregation.

For small molecule binding analysis, two startup cycles of running buffer were carried out on both surfaces after protein immobilization. Depending on observed binding kinetics, a 60–180 s association time, and a 180–360 s dissociation time at 30  $\mu\text{L}/\text{min}$  for each concentration of a particular compound over both surfaces was injected. An eight-point dose response was conducted with increasing concentrations for each compound with concentrations that were  $>10 \times K_D$  at the highest and  $<0.1 \times K_D$  at the lowest. To evaluate the binding of **5** against both CDK1 and CDK2, the concentrations employed were based on its  $K_D$  for CDK2, as **5** did not appear to bind CDK1. For **1**, the highest concentration used was 25  $\mu\text{M}$  due to nonspecific binding to the chip surface at higher concentrations. Zero concentrations were performed at the beginning and end of the dose response as a baseline and to ensure internal reproducibility. An additional maximum concentration of compound was injected after the second zero concentration as an additional internal control. Lastly, a five-point DMSO solvent correction was performed for each compound before analysis with 0.6%, 0.8%, 1.0%, 1.2%, and 1.4% DMSO in buffer. To determine the  $K_D$  and kinetic binding parameters of each compound against their respective protein, the Biacore S200 Evaluation Software (Cytiva) using affinity fit via the steady-state approximation (SSA), and when possible kinetic fit ( $k_{\text{off}}/k_{\text{on}}$ ), was used.

For protein-protein affinity analysis with cyclin, the same buffer was used but without DMSO. A single-cycle run with increasing concentrations of cyclin A was used to determine the affinity of the CDK2/cyclin A interaction due to the slow off-rate of cyclin binding. After protein immobilization, one startup run of buffer was flowed over both the reference and sample surface to equilibrate the system. In an eight-point dose response, each concentration of cyclin (0–100 nM) had a 180 s association time and 180 s dissociation time. A kinetic fit was

used to determine the  $K_D$ . For both small molecule and cyclin affinity experiments, two independent replicates were conducted.

### Förster resonant energy transfer (FRET) assay

The CDK2 FRET assay between cyclin and small molecules has been described previously<sup>29</sup>. Briefly, CDK2 (C118A C177S A93C R157C) was labeled with FRET donor and acceptor dyes (AF488, AF568; Fluorophores), purified by gel filtration, mixed with varying concentrations of bovine cyclin A and dispensed into a 384-well plate (Greiner Bio-One) into which 1  $\mu$ L inhibitor had been pre-dispensed. The final concentration of CDK2 in the FRET assays was 5 nM in 1 $\times$  PBS pH 7.4, 10 mM  $MgCl_2$ , 5 mM DTT, 0.5 mg/mL bovine gamma globulins and 0.02% Tween 20. Plates were incubated for 30 min, and measurements were performed on a fluorescence plate reader (Fluorescence Innovations). Emission peaks were spectrally unmixed<sup>54</sup>, and the ratios of the donor and acceptor peaks were used to calculate the apparent  $K_D$  for each inhibitor.

### Fluorescence interference experiments

For data generated in Supplementary Fig. 8, separately compound **5** (10  $\mu$ M) and Alexa 488 dye (5 nM) were dissolved in water (0.1% DMSO) and tested on the Horiba Fluoromax-4. The emission spectra of both compounds were obtained upon excitation at the 473 nm wavelength used for FRET. In addition, the emission spectrum of compound **5** was obtained upon excitation at 350 nm to examine its fluorescence from the indole core.

### ADP-Glo experiments

Kinase activity of phosphorylated CDK2 with different cyclin A concentrations and varying amounts of inhibitor (dinaciclib or **5**) were measured using the ADP-Glo Kinase Assay (Promega) in a luminescence plate reader (Tecan Infinite M1000 PRO). Triplicate reactions were carried out in ADP Quest Assay buffer (15 mM HEPES, pH 7.4, 150 mM NaCl, 1 mM EGTA, 0.02% Tween-20, 10 mM  $MgCl_2$ , and 0.1 mg/mL bovine- $\gamma$ -globulins). Assays were performed with 5 nM phosphorylated CDK2, 200  $\mu$ M ATP (Promega), 100  $\mu$ M PKTPPKAKKL substrate (GenScript), and varying concentrations of cyclin A (5, 50, or 500 nM). Phosphorylated CDK2 was pre-incubated with inhibitor at 20  $^{\circ}C$  for 15 min. Reactions were initiated by simultaneously adding ATP and cyclin A and incubated at 20  $^{\circ}C$  for 15 min. Reactions were then quenched with ADP-Glo reagent following the manufacturer's instruction. Luminescence was measured using a 1 s integration time and normalized to the no-inhibitor 5% DMSO controls. Kinase activity was determined by globally fitting relative luminescence data from all three cyclin A concentrations to a quadratic binding model using non-linear regression in GraphPad Prism 9. For fitting, CDK2 concentration was constrained to 5 nM with data sets from each p-CDK2:cyclin A ratio globally constrained to share the lower baseline parameter.  $IC_{50}$  values reported represent the 95% confidence intervals obtained from the fits ( $n = 3$ ) using the symmetrical likelihood method in GraphPad Prism 9.

For analogous assays with different concentrations of ATP, a similar setup was employed. Phosphorylated CDK2 (5 nM) was incubated at 20  $^{\circ}C$  for 15 min with either 83, 250, or 750  $\mu$ M ATP and varying amounts of inhibitor (dinaciclib or **5**). Peptide substrate (100  $\mu$ M) and cyclin A (5 nM) were added together to initiate the reaction and incubated at 20  $^{\circ}C$  for 30 min. Following the incubation, the reaction was quenched, and its activity measured and analyzed as above.

### Cellular thermal shift assay (CETSA)

Jurkat and OVCAR-3 cell lines were purchased from the American Type Culture Collection. Both Jurkat and OVCAR-3 cells were cultured in RPMI 1640 (Corning) medium at 37  $^{\circ}C$  in a humidified chamber under

5%  $CO_2$ . Medium for Jurkat was supplemented with 10% fetal bovine serum (Gibco) and 1% penicillin-streptomycin (Corning), and OVCAR-3 with 20% fetal bovine serum and 1% penicillin-streptomycin. The CETSA was performed following a reported protocol<sup>55</sup>. Briefly, in two separate T75 flasks for each cell line, Jurkat cells were grown to  $\sim 3$  million/mL in 10 mL medium and OVCAR-3 cells to  $\sim 1$  million/mL in 10 mL medium. Compound **5** was added to one flask for each cell line with a final concentration of 20  $\mu$ M and DMSO (0.5%) was added to the other respective flasks. Cells were incubated with the indicated treatments for 1 h (Jurkat) or 2 h (OVCAR-3) at 37  $^{\circ}C$ , then collected through centrifugation (Jurkat) or trypsinization (Gibco) followed by centrifugation (OVCAR-3). The cell pellets were then resuspended in 1 mL PBS supplemented with complete protease inhibitor cocktail (Roche) and PhosSTOP phosphatase inhibitor cocktail (Roche). For each treatment group, cells were aliquoted into ten different PCR tubes with 100  $\mu$ L of cell suspension in each tube ( $\sim 3$  million cells per tube for Jurkat and  $\sim 1$  million cells per tube for OVCAR-3). Cells in each tube were heated to their designated temperatures (40–67  $^{\circ}C$ ) for 3 min in a thermal cycler, and then the tubes were incubated at room temperature for another 3 min before snap-freeze of the samples in liquid nitrogen. Cells were fully lysed by two more cycles of freeze-thaw. The lysates were cleared by centrifugation, and an equivalent amount (12  $\mu$ L) of cell lysate from each sample was electrophoresed on a 4–12% NuPAGE gradient gel (Invitrogen) and transferred onto low fluorescent polyvinylidene difluoride membranes (Bio-Rad). Immunoblotting was performed with anti-CDK2 (sc-6248, Santa Cruz Biotechnology, 1:2000), anti-CDK1 (sc-54, Santa Cruz Biotechnology, 1:2000) and anti- $\beta$ -actin (A1978, Millipore Sigma, 1:2000) antibodies followed by secondary goat-anti-mouse (A16072, Invitrogen, 1:1000 for CDK2 and CDK1 blots) and goat-anti-mouse (A32729, Invitrogen, 1:1000 for  $\beta$ -actin blots) Alexa680 antibodies. When using horseradish peroxidase-conjugated anti-mouse antibody for CDK2 and CDK1, West Femto Maximum Sensitivity Substrate (Thermo Scientific) was added to the membranes before imaging on an Odyssey Fc Imaging system (Li-Cor). Band intensity was quantified with ImageJ 1.52a, and data were then fitted to obtain apparent  $T_{agg}$  values using the Boltzmann Sigmoid equation within GraphPad Prism (v. 9.1.1) software. Densitometry data in the melting curves are mean  $\pm$  SEM from three biological replicates.

### Cellular cyclin E1 and CDK2 quantification

For both Jurkat and OVCAR3 cell lines, 0.5 and 1 million cells were lysed in 100 mL RIPA buffer (Thermo Scientific) containing PhosSTOP phosphatase inhibitor cocktail (Roche) and complete protease inhibitor cocktail (Roche). Lysate was centrifuged at 11,000  $\times g$  for 10 min at 4  $^{\circ}C$ . Cell debris was removed and the total protein concentration normalized by a BCA assay (Pierce BCA Protein Assay Kit, Thermo Scientific). The proteins were electrophoresed on a 4–12% Bis-Tris NuPage gradient gel (Invitrogen) and transferred to a low fluorescent polyvinylidene difluoride membrane (Bio-Rad). Immunoblots were conducted with anti-cyclin E1 (#4129, Cell Signaling Technology, 1:2000), anti-CDK2 (sc-6248, Santa Cruz Biotechnology, 1:2000), and anti- $\beta$ -actin (A1978, Millipore Sigma, 1:2,000) followed by secondary horseradish peroxidase-conjugated-goat-anti-mouse (A16072, Invitrogen, 1:1,000 for cyclin E1 and CDK2 blots) and Alexa680 conjugated-goat-anti-mouse (A32729, Invitrogen, 1:1,000 for  $\beta$ -actin blots) antibodies. When using horseradish peroxidase-conjugated secondary antibody, West Femto Maximum Sensitivity Substrate (Thermo Scientific) was added to the membranes before imaging on an Odyssey Fc Imaging system (Li-Cor). Band intensity was quantified with ImageJ 1.53a and plotted in GraphPad Prism 9.3.0. Experiments were performed four times with two different cell amounts (0.5 and 1 million cells); data were aggregated to yield 8 replicates. Unpaired two-sided student's  $t$  test without adjustments was conducted to determine significance in GraphPad Prism.

### Chromosome spread preparation

For spermatocyte chromosome spreads, nine 4-month-old adult WT C57BL/6J mouse testes were dissected and incubated at 37 °C for 6 h in either Dulbecco's Modified Eagle's Medium/Nutrient Mixture F-12 (DMEM/F12, Thermo Scientific) or compound **5** (100 µM) in DMEM/F12. Following incubation, meiotic chromosome spreads were prepared as described previously<sup>36</sup>. Briefly, samples were placed in a hypotonic extraction buffer (30 mM Trizma hydrochloride, 50 mM sucrose, 17 mM sodium citrate, 5 mM EDTA, 0.5 mM DTT, and protease and phosphatase inhibitor cocktail [1:100]; Sigma-Aldrich) for 10 min. Samples were then moved to a 100 mM sucrose solution (pH 8.2) and spermatocytes were detached by pipetting. Drops of the cell suspension were then placed onto a coverslip that had previously been soaked in a 1% paraformaldehyde (Sigma-Aldrich) and 0.15% Triton X-100 (Sigma-Aldrich) solution. Coverslips were dried at room temperature overnight and either used immediately for staining or stored at -80 °C.

### Immunofluorescent staining and analysis, CDK2 Western blot

For immunofluorescent staining of chromosome spreads, slides were washed with PBS (Thermo Scientific) and 0.015% Triton X-100, blocked with 5% bovine serum albumin (Sigma-Aldrich) in PBS at room temperature for 1 h, and then incubated with anti-CDK2 monoclonal antibody (sc-6248, Santa Cruz Biotechnology, 1:100) or anti-SPY1 R55A antibody<sup>17</sup> (1:1) and anti-SYCP1 polyclonal antibody (NB300-229, Novus, 1:100), or anti-RAD51 polyclonal antibody (pc130, Millipore, 1:100) and anti-SYCP-3 monoclonal antibody (sc-74569, Santa Cruz Biotechnology, 1:100) overnight at 4 °C. Fluorescence was developed using Alexa Fluor 488 and 564 conjugated secondary antibodies (ab150073, Life Technologies, 1:250). A Nikon Eclipse TiE inverted microscope with AIR-SHR confocal was used for imaging. RAD51 localization was quantitatively assessed by determining the number of positive staining sites on the chromosome and telomeres per cell for 6 samples per group. An unpaired two-tail *t*-test with *p* < 0.05 was used to determine significance. CDK2 and SPY1 staining was qualitatively assessed through abnormal or normal scoring for 17 control samples and 6 samples treated with compound **5**, where an abnormal score was given if 3+ telomeres within the sample did not stain positive for CDK2 or SPY1. The same anti-CDK2 antibody was used for Western blot with anti-β actin antibody (Genscript, cat. # A01865) as an internal control.

### Reporting summary

Further information on research design is available in the Nature Portfolio Reporting Summary linked to this article.

### Data availability

Source data are provided with this paper, including unprocessed blots, enzyme inhibition data, and CETSA data. The data generated for Supplementary Tables 2–3 were provided by Reaction Biology via their kinase activity assays, and the data generated for Supplementary Fig. 13 were provided by Pharmaron via their cytotoxicity assays.

The crystallographic data have been deposited to the Protein Data Bank under the accession codes [7RWF](#), [7S84](#), [8FOW](#), [8FP0](#), [8FP5](#) Source data are provided with this paper.

### References

- Pan, Z. et al. Discovery of selective irreversible inhibitors for Bruton's tyrosine kinase. *ChemMedChem* **2**, 58–61 (2007).
- Teng, M. et al. Development of CDK2 and CDK5 dual degrader TMX-2172. *Angew. Chem. Int. Ed. Engl.* **59**, 13865–70 (2020).
- Jia, Y. et al. Overcoming EGFR(T790M) and EGFR(C797S) resistance with mutant-selective allosteric inhibitors. *Nature* **534**, 129–132 (2016).
- To, C. et al. Single and dual targeting of mutant EGFR with an allosteric inhibitor. *Cancer Disco.* **9**, 926–43 (2019).
- To, C. et al. An allosteric inhibitor against the therapy-resistant mutant forms of EGFR in non-small cell lung cancer. *Nat. Cancer* **3**, 402–417 (2022).
- Larkin, J. et al. Combined vemurafenib and cobimetinib in BRAF-mutated melanoma. *N. Engl. J. Med.* **371**, 1867–76 (2014).
- Flaherty, K. T. et al. Improved survival with MEK inhibition in BRAF-mutated melanoma. *N. Engl. J. Med.* **367**, 107–114 (2012).
- Dummer, R. et al. Encorafenib plus binimetinib versus vemurafenib or encorafenib in patients with BRAF-mutant melanoma (COLUMBUS): a multicentre, open-label, randomised phase 3 trial. *Lancet Oncol.* **19**, 603–15 (2018).
- Roskoski, R. Jr. Properties of FDA-approved small molecule protein kinase inhibitors: A 2021 update. *Pharm. Res.* **165**, 105463 (2021).
- Rea, D. et al. A phase 3, open-label, randomized study of asciminib, a STAMP inhibitor, vs bosutinib in CML after 2 or more prior TKIs. *Blood* **138**, 2031–41 (2021).
- Pan, Y. & Mader, M. M. Principles of kinase allosteric inhibition and pocket validation. *J. Med. Chem.* **65**, 5288–99 (2022).
- Laufkotter, O., Hu, H., Miljkovic, F. & Bajorath, J. Structure- and similarity-based survey of allosteric kinase inhibitors, activators, and closely related compounds. *J. Med. Chem.* **65**, 922–34 (2022).
- Berthet, C., Aleem, E., Coppola, V., Tessarollo, L. & Kaldis, P. Cdk2 knockout mice are viable. *Curr. Biol.* **13**, 1775–1785 (2003).
- Ortega, S. et al. Cyclin-dependent kinase 2 is essential for meiosis but not for mitotic cell division in mice. *Nat. Genet.* **35**, 25–31 (2003).
- Faber, E. B., Wang, N. & Georg, G. I. Review of rationale and progress toward targeting cyclin-dependent kinase 2 (CDK2) for male contraception. *Biol. Reprod.* **103**, 357–67 (2020).
- McGrath, D. A. et al. Structural basis of divergent cyclin-dependent kinase activation by Spyl/RINGO proteins. *EMBO J.* **36**, 2251–62 (2017).
- Mikolcevic, P. et al. Essential role of the Cdk2 activator RingoA in meiotic telomere tethering to the nuclear envelope. *Nat. Commun.* **7**, 11084 (2016).
- Merrick, K. A. et al. Switching Cdk2 on or off with small molecules to reveal requirements in human cell proliferation. *Mol. Cell* **42**, 624–636 (2011).
- Betzi, S. et al. Discovery of a potential allosteric ligand binding site in CDK2. *ACS Chem. Biol.* **6**, 492–501 (2011).
- Faber, E. B. et al. Cooperativity between orthosteric inhibitors and allosteric inhibitor 8-anilino-1-naphthalene sulfonic acid (ANS) in cyclin-dependent kinase 2. *ACS Chem. Biol.* **15**, 1759–64 (2020).
- Weber, G. & Young, L. B. Fragmentation of bovine serum albumin by pepsin: I. The origin of the acid expansion of the albumin molecule. *J. Biol. Chem.* **239**, 1415–1423 (1964).
- Stryer, L. The interaction of a naphthalene dye with apomyoglobin and apohemoglobin. A fluorescent probe of non-polar binding sites. *J. Mol. Biol.* **13**, 482–495 (1965).
- Laurence, D. J. Interactions of calf-thymus histone fractions in aqueous solution with 8-anilino-1-naphthalene-1-sulphonic acid. *Biochem. J.* **99**, 419–426 (1966).
- Brand, L., Gohlke, J. R. & Rao, D. S. Evidence for binding of rose bengal and anilino-1-naphthalenesulfonates at the active site regions of liver alcohol dehydrogenase. *Biochemistry* **6**, 3510–3518 (1967).
- Schonbrunn, E., Eschenburg, S., Luger, K., Kabsch, W. & Amrhein, N. Structural basis for the interaction of the fluorescence probe 8-anilino-1-naphthalene sulfonate (ANS) with the antibiotic target MurA. *Proc. Natl Acad. Sci. USA* **97**, 6345–6349 (2000).
- Martin, M. P. et al. A novel approach to the discovery of small-molecule ligands of CDK2. *Chembiochem* **13**, 2128–2136 (2012).

27. Faber, E. B. et al. Screening through lead optimization of high affinity, allosteric cyclin-dependent kinase 2 (CDK2) inhibitors as male contraceptives that reduce sperm counts in mice. *J. Med. Chem.* **66**, 1928–40 (2023).
28. Nepali, K., Lee, H. Y. & Liou, J. P. Nitro-group-containing drugs. *J. Med. Chem.* **62**, 2851–93 (2019).
29. Majumdar, A. et al. Allostery governs Cdk2 activation and differential recognition of CDK inhibitors. *Nat. Chem. Biol.* **17**, 456–64 (2021).
30. Wood, D. J. et al. Differences in the conformational energy landscape of CDK1 and CDK2 suggest a mechanism for achieving selective CDK inhibition. *Cell Chem. Biol.* **26**, 1–10 (2018).
31. Kim, D. M., Yang, K. & Yang, B. S. Biochemical characterizations reveal different properties between CDK4/cyclin D1 and CDK2/cyclin A. *Exp. Mol. Med.* **35**, 421–430 (2003).
32. Martinez Molina, D. et al. Monitoring drug target engagement in cells and tissues using the cellular thermal shift assay. *Science* **341**, 84–87 (2013).
33. Schmidt, T. et al. ProteomicsDB. *Nucleic Acids Res.* **46**, D1271–D1281 (2018).
34. Karlsson, M. et al. A single-cell type transcriptomics map of human tissues. *Sci. Adv.* **7**, eabh2169 (2021).
35. Parry, D. et al. Dinaciclib (SCH 727965), a novel and potent cyclin-dependent kinase inhibitor. *Mol. Cancer Ther.* **9**, 2344–2353 (2010).
36. Roskoski, R. Jr Cyclin-dependent protein kinase inhibitors including palbociclib as anticancer drugs. *Pharm. Res.* **107**, 249–75 (2016).
37. Au-Yeung, G. et al. Selective targeting of cyclin E1-amplified high-grade serous ovarian cancer by cyclin-dependent kinase 2 and AKT inhibition. *Clin. Cancer Res.* **23**, 1862–74 (2017).
38. Viera, A. et al. CDK2 is required for proper homologous pairing, recombination and sex-body formation during male mouse meiosis. *J. Cell Sci.* **122**, 2149–2159 (2009). Pt 12.
39. Tu, Z. et al. Speedy A-Cdk2 binding mediates initial telomere-nuclear envelope attachment during meiotic prophase I independent of Cdk2 activation. *Proc. Natl Acad. Sci. USA* **114**, 592–597 (2017).
40. Kalra, S., Joshi, G., Munshi, A. & Kumar, R. Structural insights of cyclin dependent kinases: Implications in design of selective inhibitors. *Eur. J. Med. Chem.* **142**, 424–58 (2017).
41. Merrick, K. A. et al. Distinct activation pathways confer cyclin-binding specificity on Cdk1 and Cdk2 in human cells. *Mol. Cell* **32**, 662–672 (2008).
42. Zhang, J. et al. Inhibition of the CDK2 and Cyclin A complex leads to autophagic degradation of CDK2 in cancer cells. *Nat. Commun.* **13**, 2835 (2022).
43. Behenna, D. C. et al. Preparation of aminopyrazolylcyclopentyl carbamate derivatives for use as CDK2 inhibitors. WO 2020157652, (2020).
44. Pauli, G. F. et al. Importance of purity evaluation and the potential of quantitative <sup>1</sup>H NMR as a purity assay. *J. Med. Chem.* **57**, 9220–9231 (2014).
45. Pauli, G. F. et al. Correction to Importance of Purity Evaluation and the Potential of Quantitative <sup>1</sup>H NMR as a Purity Assay. *J. Med. Chem.* **58**, 9061–9061 (2015).
46. Schonbrunn, E. et al. Development of highly potent and selective diaminothiazole inhibitors of cyclin-dependent kinases. *J. Med. Chem.* **56**, 3768–3782 (2013).
47. Kabsch, W. Integration, scaling, space-group assignment and post-refinement. *Acta Crystallogr. D. Biol. Crystallogr.* **66**, 133–144 (2010). Pt 2.
48. McCoy, A. J. et al. Phaser crystallographic software. *J. Appl. Crystallogr.* **40**, 658–674 (2007). Pt 4.
49. Moriarty, N. W., Grosse-Kunstleve, R. W. & Adams, P. D. electronic Ligand Builder and Optimization Workbench (eLBOW): a tool for ligand coordinate and restraint generation. *Acta Crystallogr. D. Biol. Crystallogr.* **65**, 1074–1080 (2009). Pt 10.
50. Adams, P. D. et al. PHENIX: a comprehensive Python-based system for macromolecular structure solution. *Acta Crystallogr. D. Biol. Crystallogr.* **66**, 213–221 (2010). Pt 2.
51. Emsley, P. & Cowtan, K. Coot: model-building tools for molecular graphics. *Acta Crystallogr. D. Biol. Crystallogr.* **60**, 2126–2132 (2004). Pt 12 Pt 1.
52. Chen, Z. et al. Preparation of N-(2-Arylethyl)benzylamines as antagonists of the 5-HT<sub>6</sub> receptor. WO 2002078693, (2002).
53. Wiseman, T., Williston, S., Brandts, J. F. & Lin, L.-N. Rapid measurement of binding constants and heats of binding using a new titration calorimeter. *Anal. Biochem.* **179**, 131–137 (1989).
54. Schaaf, T. M. et al. High-throughput spectral and lifetime-based FRET screening in living cells to identify small-molecule effectors of SERCA. *SLAS Disco.* **22**, 262–73 (2017).
55. Jafari, R. et al. The cellular thermal shift assay for evaluating drug target interactions in cells. *Nat. Protoc.* **9**, 2100–2122 (2014).
56. Chen, Y. et al. The SUN1-SPDYA interaction plays an essential role in meiosis prophase I. *Nat. Commun.* **12**, 3176 (2021).

## Acknowledgements

E.B.F. was supported by NIH/NIGMS (through training grants T32 GM008244 and T32 GM132029), as well as by an NIH/NCI fellowship (F30 CA232303). Funding for this project was provided by NICHD: R01 HD080431 (V.C.), R61 HD099743 (G.I.G. and V.C.), NIGMS: R01 GM121515 (N.M.L.), DOD: W81XWH-21-1-0674 (D.A.H.), W81XWH-19-1-0336 (J.T.), and Minnesota Ovarian Cancer Alliance (G.I.G.). Production of CDK1 was made possible by NIH HHSN275201800071. We acknowledge support by the GM/CA beamlines at the Advanced Photon Source (APS), funded by the National Cancer Institute (ACB-12002) and the National Institute of General Medical Sciences (AGM-12006, P30 GM138396, S10 OD012289). The APS is a U.S. Department of Energy Office of Science User Facility operated under Contract No. DE-AC02-06CH11357. The Moffitt Chemical Biology Core is acknowledged for use of the crystallization and X-ray facilities (National Cancer Institute grant P30 CA076292). We thank Dr. Tim Ward for his initial contributions to this project, Madeline Honig for help with HRMS, and Todd Rappe for help with <sup>13</sup>C NMR. We also thank Dr. Angel Nebreda for supplying the anti-SPY1 antibodies. Reaction Biology provided the data for kinase activity data in Supplementary Tables 2–3, and Pharmaron provided data for Supplementary Fig. 13.

## Author contributions

E.B.F., J.T., E.R., S.G., L.S., E.S., N.W., D.R., A.M., L.E.H., and K.J. designed experiments, acquired data, and analyzed data for this work. A.Y. and H.K. acquired data presented in this work. J.E.H., N.M.L., E.S., V.C., D.A.H., and G.I.G. helped conceive and design experiments for this work as well as analyze data.

## Competing interests

E.B.F., N.W., J.E.H., and G.I.G. are listed as inventors for a provisional patent application covering the compounds described in this paper (US Provisional Patent Application Serial No. 63/357,473—THERAPEUTIC COMPOUNDS AND METHODS—Filed June 30, 2022 (case 2021–219 Allosteric Inhibitors of Cyclin-Dependent Kinase 2 (CDK2)). The remaining authors declare no competing interests.

## Additional information

**Supplementary information** The online version contains supplementary material available at <https://doi.org/10.1038/s41467-023-38732-x>.

**Correspondence** and requests for materials should be addressed to Gunda I. Georg.

**Peer review information** *Nature Communications* thanks David Heppner, and the other, anonymous, reviewer(s) for their contribution to the peer review of this work.

**Reprints and permissions information** is available at <http://www.nature.com/reprints>

**Publisher's note** Springer Nature remains neutral with regard to jurisdictional claims in published maps and institutional affiliations.

**Open Access** This article is licensed under a Creative Commons Attribution 4.0 International License, which permits use, sharing, adaptation, distribution and reproduction in any medium or format, as long as you give appropriate credit to the original author(s) and the source, provide a link to the Creative Commons license, and indicate if changes were made. The images or other third party material in this article are included in the article's Creative Commons license, unless indicated otherwise in a credit line to the material. If material is not included in the article's Creative Commons license and your intended use is not permitted by statutory regulation or exceeds the permitted use, you will need to obtain permission directly from the copyright holder. To view a copy of this license, visit <http://creativecommons.org/licenses/by/4.0/>.

© The Author(s) 2023